

## FEDSM-ICNMM2010-' \$( ) (

### DETACHED-EDDY SIMULATIONS OF THE EFFECTS OF DIFFERENT WIND GUST MODELS ON THE UNSTEADY AERODYNAMICS OF ROAD VEHICLES

Tristan Favre\* and Gunilla Efraimsson  
Centre for ECO<sup>2</sup> Vehicle Design  
Department of Vehicle and Aeronautical Engineering  
KTH  
Stockholm  
Sweden  
Email: favre@kth.se

#### ABSTRACT

*The relative flexibility of nowadays simulation techniques offers an alternative way to experiments in order to investigate unsteady crosswind aerodynamics in an industrial framework. In this study, time-accurate simulations, Detached-Eddy Simulations (DES), are used to simulate the flow around a simple vehicle shape, the so-called Windsor model. The  $Re_L$  of the corresponding flow case is  $2.0 \cdot 10^6$ . The influence of different deterministic models of wind gusts on the aerodynamic loads and moments are studied. The wind gusts are varied in the streamwise and the vertical direction. The magnitude of the gusts models corresponds to a yaw angle of  $20^\circ$ . The aerodynamic loads calculated show a large excess of drag coupled with a reduction of the pitch moment. In addition, although the side force has a smooth variation in the gust, overshoots up to 18% higher than the steady value of yaw moment are also observed.*

#### NOMENCLATURE

A Projected frontal area.  
 $C_D$  Drag coefficient = Drag / ( $\frac{1}{2}\rho U_\infty^2 \times A$ ).  
 $C_L$  Lift coefficient = Lift / ( $\frac{1}{2}\rho U_\infty^2 \times A$ ).  
 $C_S$  Side force coefficient = Side force / ( $\frac{1}{2}\rho U_\infty^2 \times A$ ).  
 $C_{Y_{aw}}$  Yaw moment coefficient = Yaw moment / ( $\frac{1}{2}\rho U_\infty^2 \times A \times L$ ).

$C_p$  Pressure coefficient = pressure -  $p_\infty$  /  $\frac{1}{2}\rho U_\infty^2$ .  
CD 2<sup>nd</sup> order Central Difference scheme.  
h Height of the vehicle model.  
k Resolved turbulent kinetic energy.  
L Length of the vehicle model.  
LUD 2<sup>nd</sup> order Linear Upwind scheme.  
 $p_\infty$  Freestream pressure  
Q 2<sup>nd</sup> invariant of the velocity gradient.  
 $Re_L$  Reynolds number based on L.  
ST 'Steepness' of the gust model  
 $t_0$  Initial time for the gust model  
U Streamwise velocity.  
 $U_\infty$  Freestream streamwise velocity.  
V Vertical velocity.  
W Spanwise velocity.  
 $\Delta t_{gust}$  Duration of the gust (time)  
 $\rho$  Density of fluids

#### INTRODUCTION

Ground vehicles are exposed to transient crosswind from various origins such as weather, topography of the ambient environment or the surrounding traffic. The ambition to decrease the weight of ground vehicles imposes stronger needs for an enhanced understanding of the coupling between crosswind stability, the vehicle external shape and the dynamic properties. A

\*Address all correspondence to this author.

streamlined design of a car to lower the drag resistance can be a good example of this dilemma, since this design can lead to an increase in yaw moment under crosswind conditions which results in a poor handling.

Results obtained from sophisticated experimental methods have already demonstrated significant transient effects on the aerodynamic loads of ground vehicles that are exposed to unsteady crosswind gusts, [1–3]. However, the reliability and repeatability of these techniques might be difficult to ensure, e.g. the track induced vibrations perturbing the aerodynamic balance for the crosswind tracks (i.e. models propelled on a track through a wind tunnel exhaust), see [4]. Therefore, the relative flexibility of numerical methods together with the constant increase in computational resources may offer an alternative way to extensively investigate unsteady crosswind aerodynamics using methods like the Detached-Eddy Simulations (DES) also in an industrial framework. In addition, simulations provide an insight into the entire flow field which facilitates the analysis and understanding of the flow physics.

Wind gusts mainly originate from the local weather conditions, the surrounding topology or the overall traffic, although the topography is considered to be the main responsible for the gusts affecting passenger cars. This is since gusts which originate from the topography may significantly increase the local crosswind component, [5]. These types of gusts can easily be represented by deterministic gust shapes and integrated in a Computational Fluid Dynamic (CFD) simulation. On the contrary, fully turbulent wind gusts of a stochastic nature, mainly due to local weather conditions, are not yet affordable numerically.

In this report, several gust shapes, inspired from a previous experimental setup, [3,4], are introduced in a numerical domain, using time-dependant boundary conditions, seen in e.g. [6], and are therefore representative of an unsteady side wind impulse for the ground vehicle considered. The so-called Windsor model in its squareback version is considered, see Fig. 1. The same mesh topology as in [7] is used for the simulations presented in this report. Also, in [7], the influence of the cell size in the numerical mesh on the simulated flow around the Windsor model was studied in detail for headwind, steady crosswind and unsteady crosswind conditions, respectively. In this paper, the unsteady aerodynamic loads are analysed together with the development of the transient flow structures. Comparisons are made with aerodynamic loads obtained from steady crosswind simulations.

## GEOMETRY AND FLOW CASE

The Windsor model in its squareback version, which is a simple vehicle shape, Fig. 1, has the similar dimensions as the Ahmed body, e.g. [8]. The main difference between the Windsor model and the Ahmed body is the front shape, which has a more realistic design in the Windsor model and therefore seems more appropriate for crosswind studies. Indeed the front shape,

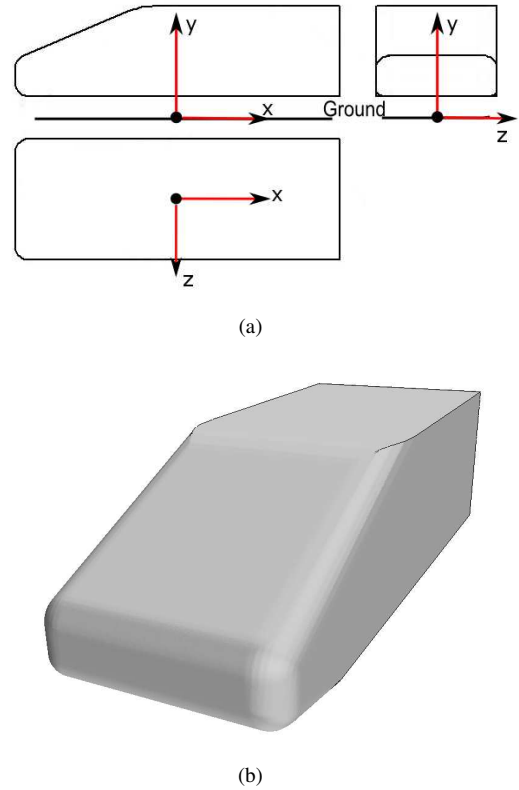


FIGURE 1. THE SQUAREBACK WINDSOR MODEL.

and especially the A-pillar with the suction observed at this location, is significantly responsible for both side force and yaw moment, [9]. In addition, all the leading edges are well rounded whereas the trailing edges are kept sharp, hence fixing the lines of separation. Numerous experimental investigations have been performed on the Windsor model where e.g. the influence of the rear design or crosswind aerodynamics have been considered. In addition, studies with or without moving ground have been conducted using different wind tunnel mounting (feet or sting), see [3, 10, 11]. No mounting devices are included in the numerical model.

The dimensions of the Windsor model is given in Table 1. In this study, the inflow velocity is the same as in [11],  $27 \text{ m/s}$ , and the crosswind velocity is taken such that the incident angle, defined as the arctangent of the crosswind speed over the vehicle velocity, is  $20^\circ$ . This yields a Reynolds number based on the vehicle length  $L$  and the air viscosity  $1.51 \times 10^{-5} \text{ m}^2/\text{s}^{-1}$   $Re_L$  of  $2.0 \cdot 10^6$ . A crosswind angle of  $20^\circ$  is believed to be a good test condition, [12], since only very extreme conditions correspond to angles higher than  $20^\circ$ .

**TABLE 1.** THE DIMENSIONS OF THE WINDSOR MODEL.

Characteristic	Size in m
Length, $L$	1.045 $m$
Width, $l$	0.390 $m$
Height, $h$	0.29 $m$
Ground Clearance	0.050 $m$
Radius of curvature, front leading edges	0.050 $m$
Radius of curvature, roof leading edge	0.200 $m$
Frontal Area, $A$	0.113 $m^2$

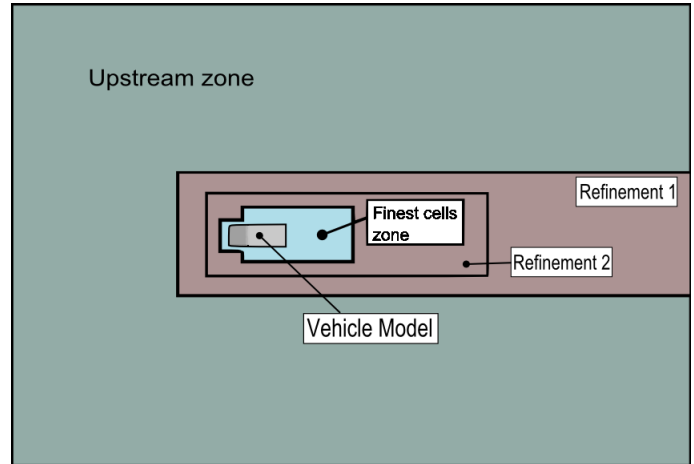
## METHODS

### Solver and Numerical Methods

The numerical simulations are performed with a commercial code, STAR-CD v4.08, developed by CD-Adapco<sup>1</sup>, which solves the Navier-Stokes equations with the finite volume method. The convective fluxes for the momentum equations are discretized using a second-order linear upwind (LUD) whereas the diffusive fluxes are discretized using central difference (CD). The turbulent equations are also discretized with LUD and the continuity equations using a blending of CD and upwind. The pressure-velocity coupling for the transient simulations is PISO, [13], modified for arbitrary control volumes by CD-Adapco. PISO in its implementation in STAR-CD provides a second-order implicit temporal discretization. The time step used in the present study is set to comply with the solver requirements for stability and is  $0.8 \cdot 10^{-4}$  s. This corresponds to an average CFL number of 0.7. The time-step value is below the minimum required for DES in [14] that is  $\Delta_0/U_{max}$ , with  $\Delta_0$  the fine cell size in the separated flows regions. As an illustration, using the finest cell size of 0.0080  $m$  for  $\Delta_0$  and approximate  $U_{max} = 1.5 \times U_{\infty}$ , [14], it leads to  $\Delta t_{min} \approx 1.9 \cdot 10^{-4}$ .

The Windsor model is placed in a computational domain as shown in Fig. 2 and 4. The rectangular block has a length in the streamwise direction of  $11L$  where  $L$  is the vehicle length, a height and a width of  $10h$  and  $20h$ , respectively, with  $h$  being the height of the vehicle. In front and behind the model, the distances are  $3.5L$  and  $6.5L$ , respectively. The computational mesh consists of unstructured polyhedral cells, [15]. The mesh topology follows the suggestions of [14] and is shown Fig. 2. A homogeneous core of fine cells is placed around the vehicle. The typical dimension of these fine cells is 0.0080  $m$  that is 2.8%  $h$ . This area extends down to  $1L$  behind the vehicle and  $0.3L$  on the sides. A fine spatial discretization is needed in this region, since there, the flow is simulated using LES (Large-Eddy Simulation),

see below. The total number of computational cells is  $9.7 \times 10^6$  which corresponds to  $56.7 \times 10^6$  faces.

**FIGURE 2.** TOPOLOGY OF THE COMPUTATIONAL MESH.

The Windsor model is described by 171 457 surface elements where the size of these surface elements corresponds to  $x^+ \approx 120$ . The solver STAR-CD uses a hybrid method that distinguishes between high- and low-Reynolds wall modelling. At the vehicle, a low-Reynolds wall modelling is applied and a  $y^+$  of 2.5 in average is found. 17 prismatic cell layers are placed around the vehicle model and the height ratio between two prismatic layers,  $y_{n+1}/y_n$ , is 1.2. An average of 9 cells are below  $y^+ = 11.5$ . On the ground, a high-Reynolds wall modelling is desired and a  $y^+$  of 30 in average is created.

The DES uses the Spalart-Allmaras (S-A) model, [16], as the RANS model. The actual version of DES used is the extension of this model to be resistant to ambiguous grid design called Delayed-DES, (D-DES). It prevents the LES mode to be activated and enforce RANS close to the walls, [17]. The adjustable constant  $C_{DES}$  and is set at 0.65 in the code.

The DES simulations are initialized using prior RANS simulations. The  $k - \omega$  SST turbulence model from [18] was set together with the SIMPLE, [19], for the velocity-pressure coupling. The LUD scheme was used for the discretization in space. After 2000 iterations, all simulations were converged to steady state, all the residuals were below  $10^{-4}$ .

### Boundary Conditions for Unsteady Wind Gusts

The objective of this study is to perform a parameter study for the gust scenario simulated. In the experiment of [4], a cross-wind track is used in which a vehicle is propelled at a constant speed through a wind tunnel exhaust. It is represented by a

<sup>1</sup>www.cd-adapco.com

smooth step function that has cosine functions to model the entrance and exit mixing zones, Fig. 3.

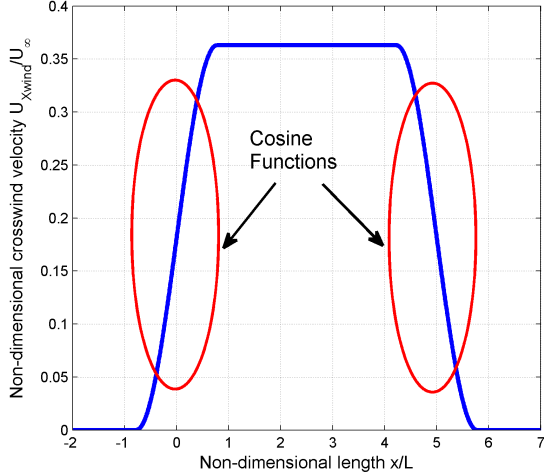


FIGURE 3. THE WIND GUST SCENARIO.

The maximum speed of the gust,  $9.8 \text{ m/s}$ , corresponds to  $20^\circ$  yaw angle (arctangent of the crosswind speed over the vehicle velocity). The choice of a cosine functions modelling the mixing zone at the entrance and exit of the gust is justified by the measurements reported in [20] that demonstrates that the mixing zone at a jet flow is described by a cosine function.

A ground moving only in the streamwise direction is used throughout the simulations. A side inlet is created in addition of the traditional front inlet, Fig. 4, in order to introduce a time-dependent velocity profile. The wind profile is then a function of space and time. The opposite side and the rear surface are pressure outlet. The top surface is set to symmetry.

At the inlet boundary, the expression for the spanwise (crosswind) velocity  $W$  is:

$$W(t) = \begin{cases} 0 & \text{for } t < t_0 - ST/2 \\ 9.8 \cdot \frac{1}{2} (1 - \cos \left[ \frac{(t - (t_0 - ST/2)) \pi}{ST} \right]) & \text{for } t_0 - ST/2 < t < t_0 + ST/2 \\ 9.8 & \text{for } t_0 + ST/2 < t < t_0 + \Delta t_{gust} - ST/2 \\ 9.8 \cdot \frac{1}{2} (1 - \cos \left[ \frac{(t - (t_0 + \Delta t_{gust} + ST/2)) \pi}{ST} \right]) & \text{for } t_0 + \Delta t_{gust} - ST/2 < t < t_0 + \Delta t_{gust} + ST/2 \\ 0 & \text{for } t > t_0 + \Delta t_{gust} + ST/2 \end{cases} \quad (1)$$

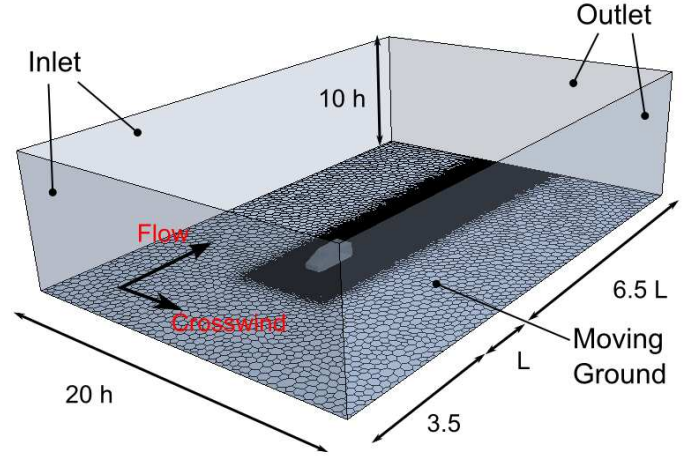


FIGURE 4. THE COMPUTATIONAL DOMAIN AND THE BOUNDARY CONDITIONS.

At the side-inlet, the crosswind velocity  $W$  is function of space and time:

$$W(x,t) = \begin{cases} 0 & \text{for } x < U_\infty(t_0 - ST/2) \\ 9.8 \cdot \frac{1}{2} (1 - \cos \left[ \frac{(x - U_\infty(t_0 - ST/2)) \pi}{U_\infty ST} \right]) & \text{for } U_\infty(t_0 - ST/2) < x < U_\infty(t_0 + ST/2) \\ 9.8 & \text{for } U_\infty(t_0 + ST/2) < x < U_\infty(t_0 + \Delta t_{gust} - ST/2) \\ 9.8 \cdot \frac{1}{2} (1 - \cos \left[ \frac{(x - U_\infty(t_0 + \Delta t_{gust} + ST/2)) \pi}{U_\infty ST} \right]) & \text{for } U_\infty(t_0 + \Delta t_{gust} - ST/2) < x < U_\infty(t_0 + \Delta t_{gust} + ST/2) \\ 0 & \text{for } x > U_\infty(t_0 + \Delta t_{gust} + ST/2) \end{cases} \quad (2)$$

The time  $t_0$  is the 'initial' time of the gust, defined when  $W(x,t) = W/2$  for the implementation.

From the gust scenario shown in Fig. 3 and called *baseline* from now, three parameters are extracted: the period of the cosine function  $ST$  (describing the steepness of the gust), the total duration of the gust  $\Delta t_{gust}$  (or streamwise extension) and the vertical profile. The baseline steepness of the gust is arbitrarily chosen to be  $1.5L/U_\infty$ . Two additional steepnesses are tested, one shorter  $1L/U_\infty$ , *WG1*, and one longer  $5L/U_\infty$ , *WG2*. For the total duration, the baseline is set as in the experiment of [4]. It is seen in [21] that the ratio between a passenger car and a typical gust length is around 7; therefore, a gust of duration  $7L$  is tested, *WG5*. All the parameters are reported in Table 2.

Finally, for *WG6*, a vertical profile is implemented and is

**TABLE 2.** GUST PARAMETERS.

Gust models	$\Delta t_{gust}$	$ST$
Baseline	$\frac{5 \cdot L}{U_\infty}$	$\frac{1.5 \cdot L}{U_\infty}$
WG1	$\frac{5 \cdot L}{U_\infty}$	$\frac{1 \cdot L}{U_\infty}$
WG2	$\frac{5 \cdot L}{U_\infty}$	$\frac{5 \cdot L}{U_\infty}$
WG6	$\frac{7 \cdot L}{U_\infty}$	$\frac{1.5 \cdot L}{U_\infty}$
WG6	$\frac{7 \cdot L}{U_\infty}$	$\frac{1.5 \cdot L}{U_\infty}$

represented by a simple exponential function describing an ideal flat terrain, see [22]:

$$W(x, y, t) = W(x, t) \left( \frac{y}{y_{ref}} \right)^{0.12}, \quad (3)$$

A reference velocity  $W(x, t)$ , at a reference height  $y_{ref}$ , has to be given in (3). The reference height is chosen such that a gust velocity of  $9.8 \text{ m/s}$  is obtained at the mid height of the vehicle, that is at  $0.195 \text{ m}$ .

In addition of Fig. 3, the windgust profiles are plotted in Fig. 5. Note that WG2 is equivalent to a full cosine shape. The x-axis represent the streamwise extension of the gust and non-dimensionalized by the vehicle length  $L$ .

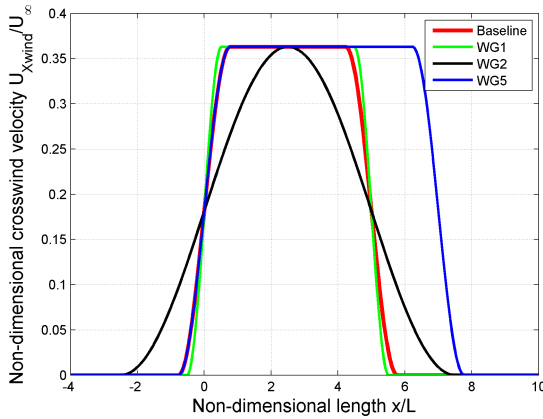


**FIGURE 5.** THE WINDGUSTS MODELS CONSIDERED IN THIS STUDY.

## RESULTS AND DISCUSSIONS

The coordinate system used for calculating the moments, see Fig. 1(a), is located on the ground ( $y = 0$ ), and at the centre of the vehicle  $1/2L$  and  $1/2l$ . The axes are oriented such that a positive pitch means that the front tends to go down, a positive roll means that the vehicle tends to roll away from the gust and a positive yaw means that the vehicle tends to steer away from the gust.

The time dependent wind gusts were introduced as boundary data after 290 time units  $t^* = tU_\infty/\sqrt{A}$  (which is approx. 46000 time steps) of head wind simulations. This corresponds that the flow has ran 9 times through the whole computational domain.

Considering the force coefficients calculated, the dynamic pressure is calculated taking the vehicle and the crosswind velocities into account,  $\sqrt{27^2 + 9.8^2}$ .

### Single transient wind gust

The loads from the different wind gusts are shown in Fig. 6, for a gust length of  $5L$ . The values for  $C_{Side}$  and  $C_{Yaw}$  from steady crosswind DES [7] are added. In [7] a similar mesh to the one used in this study is utilized and the upstream zone (see Fig. 2) is coarser than the present one. However, it is seen in [7] that the side force and the yaw moment are not affected by the change and hence used in this study for comparison.

From Fig. 6, it is observed for the baseline scenario that  $C_{Side}$  tends to the steady value. No overshoot is found. A similar results is found by the authors when simulating a radiused model of a box (REVM) in [23]. It seems that the radius of curvature prevents all the overshoot for  $C_{Side}$  and smoother variations are observed.

On the other hand,  $C_{Yaw}$  exhibits a strong and clear overshoot after the vehicle entered the gust. It is noticeable for the baseline, the peak is 12% higher than the steady value. After approximately  $2L$  in the gust, the  $C_{Yaw}$  stabilized at a level equivalent to the steady value. Similar behaviours are found in [1, 2, 4, 23] for slightly different geometries (box-like models) but similar gust. Figs. 7 and 8 show the flow field as well as the pressure coefficient on the leeward sides at the peak of yaw moment (Fig. 7), and just after, when  $C_{Yaw}$  has stabilized (Fig. 8).

The coherent structures of the flow, defined in e.g. [24], are investigated by using the second invariant of the velocity gradient, the so-called  $Q$  criterion. The second invariant of the velocity gradient  $\Delta \mathbf{u}$  is defined for incompressible flow as

$$Q = \frac{1}{2} (\|\boldsymbol{\Omega}\|^2 - \|\mathbf{S}\|^2) \quad (4)$$

where  $\|\boldsymbol{\Omega}\|^2 = tr[\boldsymbol{\Omega}\boldsymbol{\Omega}^t]^{1/2}$  and  $\|\mathbf{S}\|^2 = tr[\mathbf{S}\mathbf{S}^t]^{1/2}$ ;  $\mathbf{S}$  and  $\boldsymbol{\Omega}$  are the symmetric and antisymmetric component of  $\Delta \mathbf{u}$ . Thus  $Q$  can be seen as the local balance between the rotation rate relative to the strain rate. Positive and high values of  $Q$  correspond to a high level of flow vorticity. [25] demonstrates that this is a necessary

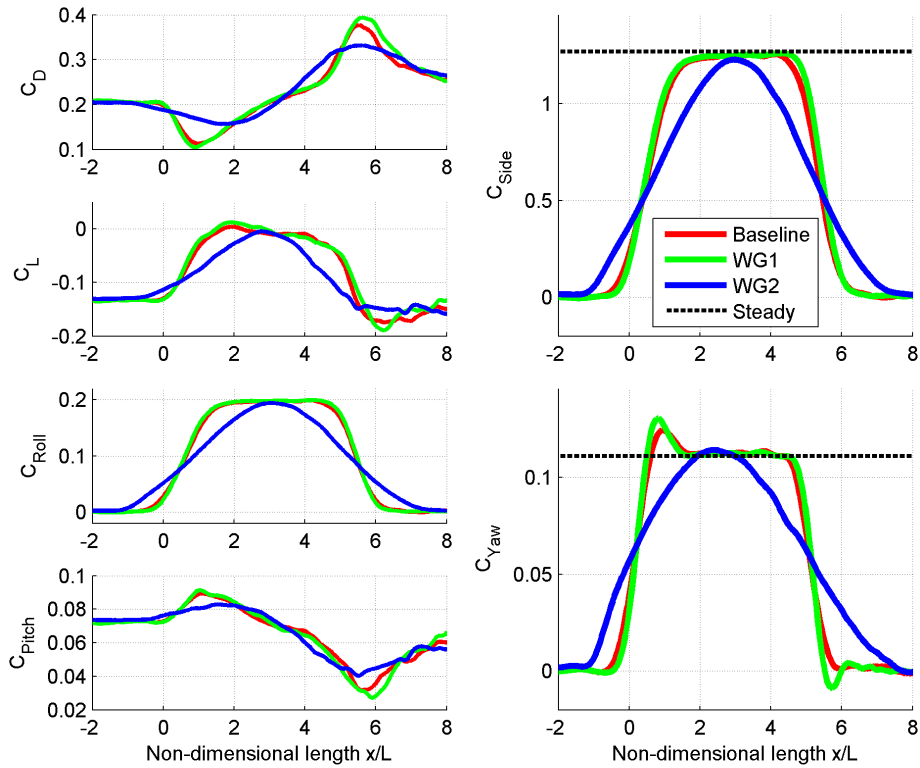


FIGURE 6. TIME HISTORY OF THE AERODYNAMIC LOADS.

condition for vortex cores. In addition, to ensure a sufficient condition, the pressure shall decrease in this area of the flow. More details on the theoretical aspects regarding flow visualization can be found in [26]. However, it should be pointed out that the pressure condition is subsumed in  $Q > 0$ .

A few differences are observed in the flow fields. First, the flow structures on the leeward side, mainly two vortices, are not fully developed yet at the time when the peak occurs in  $C_{Yaw}$ . Although the roof vortex has appeared and the car has entered the gust for more than  $1L$ , highlighted area B in Fig. 7, its interaction with the wake has further strengthened for a later time, see area B in Fig. 8. The peak in yaw moment is then explained by a higher contribution from the front of the vehicle illustrated by the pressure distribution on the leeward side: at the peak, the area of low pressure is more focused to the front whereas after the peak the low pressure is more spread over the body.

The change of the front pressure distribution, especially the very low negative pressure ( $C_p < -2$ ) at the leeward front-pillar, yields a decrease of drag. After approx.  $1L$  in gust, the decrease of drag due to the drop of front pressure is compensated by the leeward vortices and the perturbed wake. Hence, the drag is ut-

terly increasing (up to +88%). The drag peaks due to the combination of the reestablishment of the front headwind pressure distribution and the crosswind wake.

The lift tends to increase with the appearance of the leeward crosswind vortices. The collapse of the crosswind flow provokes a steep drop of lift.

### System parameters study

In this section, the loads for WG1, WG2, WG5 and WG6, respectively, are compared and analysed. In additions of Fig. 6, Fig. 9 shows the loads from baseline and the gusts of lengths  $7L$ . First, from Figs. 6 and 9, it is seen that the time histories of the forces follow a similar pattern for all the gusts studied. After entering the gust, the change of front pressure lowers the drag but increases the lift and pitch moment. While the vehicle is fully in the gust and the leeward structures develop, the pitch decreases and the drag increases in turn. The latter has a peak short after the gust exit when the headwind front pressure penalty cumulates with the influence of the crosswind wake. The wind gust has an opposite effect on the drag and on the pitch moment. The values of the peaks are very large compared to the values before the gust.

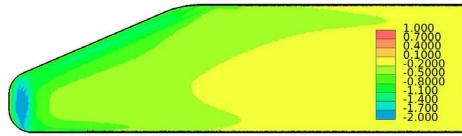


**FIGURE 7.** PRESSURE AND FLOW STRUCTURES ( $Q = 50000$ ) AT PEAK IN THE YAW HISTORY ( $x/L \approx 1$  IN FIG.6).

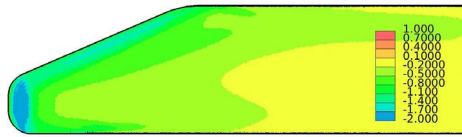


**FIGURE 8.** PRESSURE AND FLOW STRUCTURES ( $Q = 50000$ ) WHEN THE YAW IS STABILIZED ( $x/L > 2$  IN FIG.6).

The peaks for baseline, WG1 and WG2 are reported in Table 3. For the baseline gust, the drag increases up to 80% of its original value whereas the pitch decreases by 56%.

Making the gust 33% steeper, WG1 and Fig. 6, leads to higher peaks in the aerodynamic loads, at the exit for  $C_{Yaw}$  (18%

**TABLE 3.** MAJOR PEAKS IN THE COMPUTED LOADS.

Gust models	$C_{Yaw}$	$C_D$	$C_{Pitch}$
Baseline	12%	80%	-56%
WG1	18%	88%	-63%
WG2	3%	58%	-44%

instead of 12%) or at the exit for  $C_D$  (88% instead of 80%) and  $C_{Pitch}$  (-63% instead of -56%). As expected, the loads exhibit higher rates of increase and decrease. Changing the gust profile to a full cosine shape, WG2, shows the similar trend in the loads' time histories, Fig. 6.

The results presented in Fig. 9 shows that the loads of the longer gusts exhibit stronger fluctuations in the gusts after approx.  $4L$  (especially visible for  $C_{Yaw}$ ). Also, the vertical profile is altered with WG6. In general, lower values for the loads are observed. However, the peaks in drag and pitch moment at the gust exit are similar to WG5's.

To analyse the flow during the gusts, the rms (root mean square) values for the three velocities are calculated for the period of the time when the vehicle is exposed to the gusts, that is  $t = ST + \Delta t_{gust}$  ( $\approx 0.1935 s \approx 2420$  time steps) or  $t = \frac{7L}{U_\infty}$ . We define the *resolved turbulent kinetic energy* ( $k$ ) as  $k = \frac{\langle u^2 + v^2 + w^2 \rangle}{2U_\infty^2}$  ( $u, v$  and  $w$  designed the fluctuations of the velocity components  $U, V$  and  $W$ ). In Fig. 10, iso-surfaces of are shown for a selection of 4 gusts corresponding to a high value  $k = 0.1$ . It is directly observed that the leeward area where two vortices are found in the flow do not produce large value of  $k$  during the gust.

The steeper gust (WG1) that produces higher drag and yaw moment, see Fig. 6, also exhibits larger area and higher peaks of  $k$ . The iso-surface of the longest gust (WG5) that exhibits higher larger oscillations during crosswind in Fig. 9, is also larger than the baseline's. Finally, it is seen that the smoother gust (WG2) has lower level of  $k$ . It is also observed that the interaction from the roof vortex and the wake is much less pronounced than the other gusts.

Figure 11 shows a plot of  $k$  for the sections  $y/h = 0.3$  and  $y/h = 0.8$  and for the same 4 gusts discussed above. For convenience, the height  $y/h = 0$  corresponds to the vehicle's floor (hence the ground is located at  $y/h = -0.17$ ). The section  $y/h = 0.8$ , Fig. 11(b) corresponds to approx. at the height of the upper leeward vortex when it reaches the wake. From Fig. 11,  $k$  is seen more intense in the wake than on the leeward side. More intense levels of  $k$  are also found for WG1 compare to the baseline. As guessed from Fig. 10 with the iso-surface  $k = 0.1$ , the region in the wake close to the ground reveals to be a large area

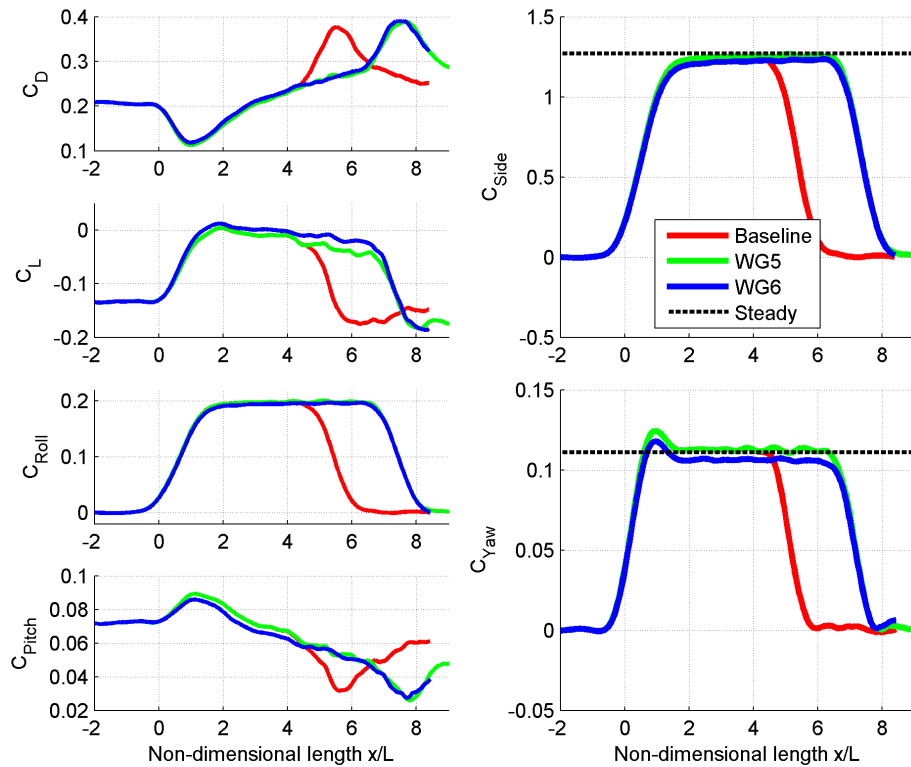


**FIGURE 9.** TIME HISTORY OF THE AERODYNAMIC LOADS.

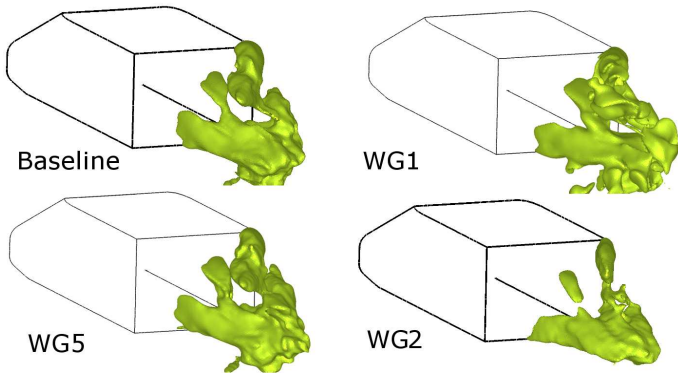


**FIGURE 10.** ISO-SURFACES OF NON-DIMENSIONAL RESOLVED TURBULENT KINETIC ENERGY ( $k=0.1$ ) FOR DIFFERENT GUSTS.

where the turbulent kinetic energy is high. The plot of  $k$  in the section  $y/h = 0.3$ , Fig. 11(a) confirms large and high level of  $k$  closer to ground, where the flow originating from the underbody

interacts with the crosswind wake. Once again, the highest values of  $k$  are found for WG2. Lower levels are observed for WG2.

The role of the roof vortex can hence be discussed. When the crosswind flow is established, approx. after  $2L$  in the gust, the flow at the leeward side is mostly responsible for the values of the aerodynamic loads. The side of the vehicle has a forward low pressure area, see Fig. 8, and leads to high side force and yaw moment. In Fig. 10, the iso-surface  $k = 0.1$  for the baseline, WG2 and WG5 show that long gust times yield the development of the interaction of the roof vortex - wake, and therefore higher levels of  $k$ . It is then not surprising to observe higher peak of drag for a long gust (WG5).

## CONCLUSION

Some conclusions can be drawn from the parameter study concerning one wind gust scenario for a generic road car.

The overall behaviour of the loads follows a similar trend for all the wind gusts considered. Smooth variations in the side force history are observed, partly explained by the well rounded edges in the model's front.

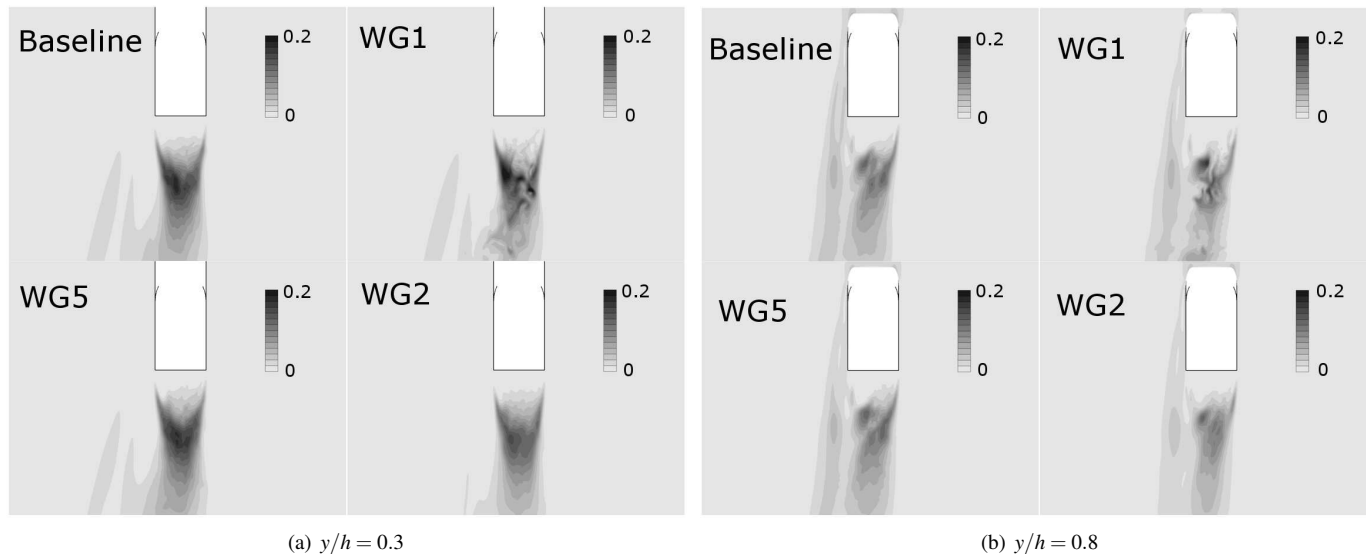


**FIGURE 11.** SECTIONS OF NON-DIMENSIONAL RESOLVED TURBULENT KINETIC ENERGY FOR DIFFERENT GUSTS.

The drag and pitch moment have an opposite behaviour when exposed to a gust. Both exhibit very large peaks at gust exit: the drag increases up to 88% whereas the pitch decreases down 63%.

Overshoots up to 18% higher than the steady value are observed for the yaw moment at gust entrance.

In general, the steeper the gust, the larger the peaks. This is noticeable for  $C_{Yaw}$ ,  $C_D$  and  $C_{Pitch}$ .

When the crosswind flow is established, the leeward side plays a dominant role for the loads. The distribution of pressure on the leeward side determines the amount of side force for the model.

The interaction between the roof vortex and the wake has a direct influence on the development of aerodynamic loads, especially for long gusts.

Finally, further investigations concerning the model's design are enabled by the crosswind scenarios summarized in this paper. Significant improvements on the model's crosswind characteristics would be achieved by finding the alterations that would lower the excess of drag and limit the yaw moment.

## ACKNOWLEDGMENT

This study is carried out within the crosswind project of the Centre for ECO<sup>2</sup> Vehicle Design. The study has benefited from computing resources at the Centre for Parallel Computers (PDC), KTH Sweden, which are granted by the Swedish National Infrastructure for Computing (SNIC).

## REFERENCES

- [1] Baker, C. J., 1986. "Train aerodynamic forces and moments from moving model experiments". *Journal of Wind Engineering and Industrial Aerodynamics*, **24**, pp. 227–251.
- [2] Kobayashi, N., and Yamada, M., 1988. "Stability of a one box type vehicle in a cross-wind - an analysis of transient aerodynamic forces and moments". *SAE Technical Paper Series*. 881878.
- [3] Cairns, R. S., 1994. "Lateral aerodynamics of motor vehicles in transient crosswinds". PhD Thesis, College of Aeronautics, Cranfield University, UK.
- [4] Chadwick, A., Garry, K., and Howell, J., 2001. "Transient aerodynamic characteristics of simple vehicle shapes by the measurement of surface pressures". *SAE Technical Paper Series*. 2001-01-0876.
- [5] Narita, N., 1981. "Gusty wind effects on driving safety of road vehicles". *Journal of Wind Engineering and Industrial Aerodynamics*, **9**, pp. 181–191.
- [6] Docton, M., and Dominy, R., 1996. "The simulation of transient cross winds on passenger vehicles". In *MIRA International Vehicle Aerodynamics Conference*, MIRA, ed.
- [7] Favre, T., 2009. "Numerical investigation of unsteady crosswind aerodynamics for ground vehicles". Lic. Tech. Thesis, Aeronautical Engineering, KTH, Sweden.
- [8] Ahmed, S. R., Ramm, G., and Faltin, G., 1984. "Some salient features of the time-averaged ground vehicle wake". *SAE Technical Paper Series*. 840300.
- [9] Howell, J. P., 1996. "The side load distribution on a rover 800 saloon car under crosswind conditions". *Journal of Wind Engineering and Industrial Aerodynamics*, **60**,

pp. 139–153.

[10] Howell, J. P., 1993. “Shape features which influence crosswind sensitivity”. In The Institution of Mechanical Engineers, IMechE 1993-9, Vehicle Ride and Handling.

[11] Howell, J. P., and Good, G. L., 2005. “Vortex drag for a simple bluff body at incidence in ground proximity”. *SAE Technical Paper Series*. 2005-01-0869.

[12] Hucho, W.-H., 1998. *Aerodynamics of Road Vehicles*. SAE International.

[13] Issa, R. I., 1985. “Solution of the implicitly discretised fluid flow equations by operator-splitting”. *Journal of Computational Physics*, **62**, pp. 45–65.

[14] Spalart, P. R., 2001. Young-person’s guide to Detached-Eddy Simulation grids. Technical report, NASA. NASA CR 2001-211032.

[15] Peric, M., 2004. “Flow simulation using control volumes of arbitrary polyhedral shapes”. *Ercoftac Bulletin*, **62**, pp. 25–29.

[16] Spalart, P. R., and Allmaras, S., 1992. “A one-equation model for aerodynamic flows”. In AIAA 30<sup>th</sup> Aerospace Sciences Meeting, Reno, NV, AIAA, ed. AIAA Paper 92-0439.

[17] Spalart, P. R., Deck, S., Shur, M. L., Squires, S. D., Strelets, M. K., and Travin, A., 2006. “A new version of detached-eddy simulation, resistant to ambiguous grid densities”. *Theoretical Computational Fluid Dynamic*, **20**, pp. 181–195.

[18] Menter, F. R., 1992. Improved two-equation  $k - \omega$  turbulence models for aerodynamic flows. Technical memorandum, NASA. 103975.

[19] Patankar, S. V., and Spalding, D. B., 1972. “A calculation procedure for heat, mass and momentum transfer in three-dimensional parabolic flows”. *Int. J. Heat Mass Transfer*, **15**, pp. 1787–1806.

[20] Schlichting, H., 1960. *Boundary Layer Theory*. McGraw-Hill series in mechanical engineering.

[21] Cooper, R. K., 1984. “Atmospheric turbulence with respect to moving ground vehicles”. *Journal of Wind Engineering and Industrial Aerodynamics*, **17**, pp. 215–238.

[22] Dyrbye, C., and Hansen, S. O., 1997. *Wind Loads on Structures*. John Wiley and Sons. ISBN 0471956511.

[23] Favre, T., Efraimsson, G., and Diedrichs, B., 2008. “Numerical investigation of unsteady crosswind vehicle aerodynamics using time-dependent inflow conditions”. In Seventh World MIRA International Vehicle Aerodynamics Conference, MIRA, ed.

[24] Hussain, F., 1986. “Coherent structures and turbulence”. *Journal of Fluid Mechanics*, **173**, pp. 303–356.

[25] Jeong, J., and Hussain, F., 1995. “On the identification of a vortex”. *Journal of Fluid Mechanics*, **285**, pp. 69–94.

[26] Chakraborty, P., Balachandar, S., and Adrian, J., 2005. “On the relationships between local vortex identification

schemes”. *Journal of Fluid Mechanics*, **535**, pp. 189–214.